The Impact of Hail Size on Simulated Supercell Storms

SUSAN C. VAN DEN HEEVER AND WILLIAM R. COTTON

Colorado State University, Fort Collins, Colorado

(Manuscript received 14 November 2002, in final form 15 January 2004)

ABSTRACT

Variations in storm microstructure due to updraft strength, liquid water content, and the presence of dry layers, wind shear, and cloud nucleating aerosol concentrations are likely to lead to changes in hail sizes within deep convective storms. The focus of this paper is to determine how the overall dynamics and microphysical structure of deep convective storms are affected if hail sizes are somehow altered in a storm environment that is otherwise the same. The sensitivity of simulated supercell storms to hail size distributions is investigated by systematically varying the mean hail diameter from 3 mm to 1 cm using the Regional Atmospheric Modeling System (RAMS) model. Increasing the mean hail diameter results in a hail size distribution in which the number concentration of smaller hailstones is decreased, while that of the larger hailstones is increased. This shift in the hail size distribution as a result of increasing the mean hail diameter leads to an increase in the mean terminal fall speed of the hail species and to reduced melting and evaporation rates. The sensitivity simulations demonstrate that the low-level downdrafts are stronger, the cold pools are deeper and more intense, the left-moving updraft is shorter-lived, the right-moving storm is stronger but not as steady, and the low-level vertical vorticity is greater in the cases with smaller hail stones. The maximum hail mixing ratios are greater in the larger hail simulations, but they are located higher in the storm and farther away from the updraft core in the smaller hail runs. Changes in the hail size distribution also appear to influence the type of supercell that develops.

1. Introduction

It may be expected that variations in storm microstructure due to updraft strength, liquid water content, the presence of dry layers, wind shear, and cloud nucleating aerosol concentrations [cloud condensation nuclei (CCN), giant CCN (GCCN), and ice-forming nuclei (IFN)] will lead to changes in hail sizes within deep convective storms. Changes in hail sizes may in turn influence the dynamical and microphysical characteristics of these storms. The focus of this paper is to determine how the overall dynamics and microphysical structure of deep convective storms are affected if the hail sizes are somehow altered in a storm environment that is otherwise the same.

Experiments designed to investigate the sensitivity to including the ice phase in mesoscale models have demonstrated significant impacts on both the dynamic and precipitation characteristics of simulated deep convective storms (e.g., Chen and Cotton 1988; Jewett et al. 1990; Johnson et al. 1993; Tartaglione et al. 1996; Schlesinger 1999; Gilmore et al. 2004). While the impacts of including the ice phase have been investigated to some degree, very little attention has been given as to how the way in which the ice phase is parameterized affects the characteristics of simulated deep convective storms, with the possible exception of Meyers et al. (1997) and Gilmore et al. (2004).

Selecting which hydrometeor species to represent and determining an appropriate size distribution for each species are examples of some of the options that need to be considered when using a single-moment bulk microphysical parameterization scheme, a type of microphysical scheme often used in mesoscale and cloud models. Ice parameters also need to be set for a broad range of storm systems if the model is to be used operationally where ''tweaking'' of the parameters is not an option. Determining suitable values for microphysical parameters is made difficult by the lack of in situ cloud data and the fact that the values can vary significantly from one storm system to another. As a result of these difficulties, microphysical parameter values are often chosen somewhat arbitrarily.

The use of a single-moment microphysical scheme necessarily results in certain characteristics of the hydrometeor size distribution having to be fixed throughout the model domain for the duration of the simulation. The mean hydrometeor diameter may be held fixed while the number concentration intercept is diagnosed, or the intercept parameter may be specified and the mean hydrometeor diameter is then diagnosed. However, the use of a single-moment scheme, unlike the more so-

Corresponding author address: Susan C. van den Heever, Dept. of Atmospheric Sciences, Colorado State University, Fort Collins, CO 80523-1371.
E-mail: sue@atmos.col.state.edu

phisticated two-moment bulk microphysical schemes, does allow for the direct control of the hail size, and hence for the investigation of the sensitivity of storm dynamics to these hail size variations.

Given the importance of understanding how changes in hailstone size and the microphysical structure of clouds may alter hailstorm dynamics, the apparent significance of including the ice phase in numerical simulations of deep convective storms, and the difficulty in determining appropriate values of various ice parameters, it is essential that we understand the sensitivity of simulated storm characteristics to variations in hailstone size distribution characteristics. The purpose of the research presented in this paper is therefore to determine the impact that changes in the hail size distribution may have on simulated deep convective storms. In particular, the following two questions will be addressed.

1) Does varying the mean hail diameter have an impact on the basic dynamic, thermodynamic, and precipitation characteristics of simulated supercell storms?
2) If so, what are the impacts and why do they occur?

To address these questions, the mean hail diameter was systematically varied, and the spectrum of simulated supercell storm characteristics that developed was investigated. It will be shown in this paper that storm longevity, the cold pool dynamics, the amount and type of precipitation, the distribution of precipitation with respect to the updraft, the low-level vertical vorticity, and the type of storm that develops are all sensitive to variations in the mean hail diameter.

The mesoscale model used to conduct the sensitivity experiments, several microphysical parameterization aspects, and the experiment design are described in section 2. The results of varying the mean hail diameter will be presented in section 3. A discussion of the implications of these results is included in section 4.

2. Model and experiment setup

a. Model configuration

The Regional Atmospheric Modeling System (RAMS; Pielke et al. 1992; Cotton et al. 2003) developed at Colorado State University (CSU) was used to achieve our stated goal. A single model grid (140 × 170 × 35) with grid spacing of 1 km in the horizontal and variable spacing in the vertical was employed. The lowest vertical grid spacing was 100 m, and this was stretched using a stretch ratio of 1.1 until the vertical grid spacing reached 2000 m, above which it was kept constant. The model top extended beyond 23 km above ground level (AGL), and there were nine model levels within the first kilometer AGL. These grid spacings are sufficient to resolve storm-scale features and processes, but are insufficient to simulate tornadogenesis. The long time step was 5 s. The basic radiative condition was applied at the lateral boundaries (Klemp and Wilhelmson 1978a), a Rayleigh friction layer was extended from approximately 17.5 km AGL to the model top to absorb gravity waves, and the lower boundary was free slip. A single-moment bulk microphysical scheme (Walko et al. 1995) was used, and all the water species were activated. The details of the model configuration are summarized in Table 1.

TABLE 1. RAMS model configuration and options.

Model aspect	Setting
Grid	Arakawa C grid Single grid Horizontal grid: $\Delta x = \Delta y = 1$ km 140 points × 170 points Vertical grid: Δz variable 35 vertical levels Model top: ~23 km Nine levels below 1 km AGL
Initialization	Horizontally homogeneous
Time step	5 s
Simulation duration	2 h
Microphysics scheme	Single-moment bulk microphysics Water species: vapor, cloud water, rain, pristine ice, snow, aggregates, graupel, and hail all activated
Convective initiation	Warm, moist bubble
Boundary conditions	Radiative lateral boundary (Klemp and Wilhelmson 1978a) Rigid lid at model top with Rayleigh friction layer Free-slip lower boundary
Turbulence scheme	Smagorinsky (1963) deformation K

The model domain was initialized horizontally homogeneously using a sounding that is typical of severe storm days over Oklahoma (Fig. 1). A similar sounding was used by Grasso (2000). The sounding is characterized by 3130 J of convective available potential energy (CAPE) and veering winds from the surface to 2 km AGL. The lifting condensation level occurs at approximately 840 mb. Convection was initiated using a warm (3-K temperature perturbation), moist (20% moisture perturbation) rectangular bubble that was 10 km by 10 km ($x = 30$ to 40, $y = 30$ to 40) in the horizontal (the position of which is indicated on Fig. 3), and which extended from the surface to approximately 2.5 km AGL. All the simulations were run for at least 2 h.

b. Microphysical parameterization considerations and experiment design

All the available hydrometeor species (cloud water, rain, pristine ice, snow, aggregates, graupel, and hail) of the single-moment bulk microphysical scheme in RAMS were activated for the sensitivity tests conducted here (Walko et al. 1995). The Marshall–Palmer (exponential) size distribution was used for all species (Marshall and Palmer 1948). This size distribution is fre-

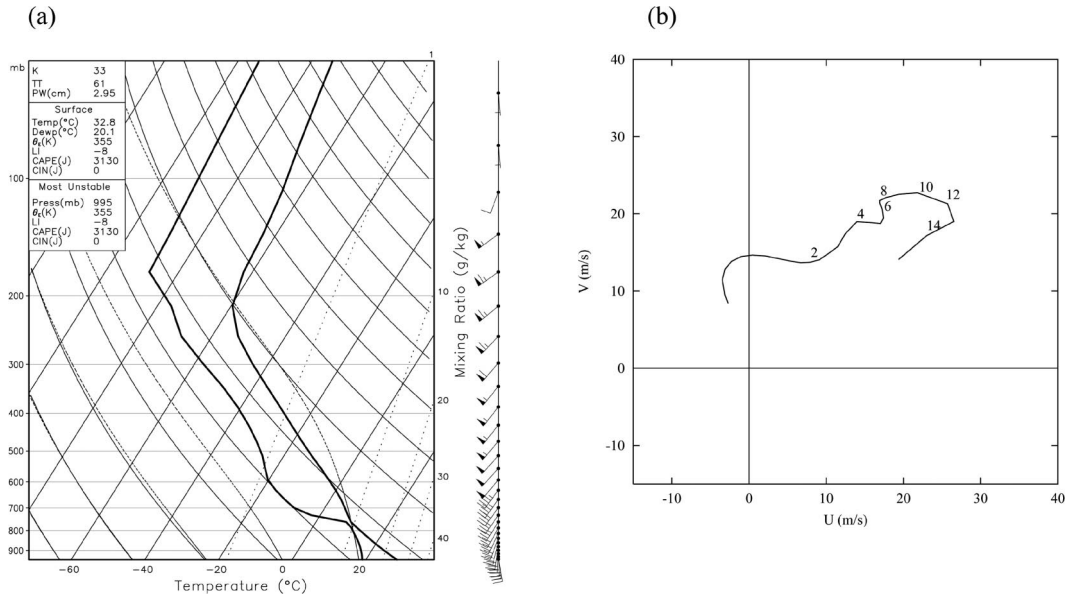

FIG. 1. (a) Sounding and (b) hodograph utilized in all of the sensitivity tests. Numbers on the hodograph indicate heights (km) AGL.

quently used in other microphysical parameterization schemes and thus provides some basis for comparison. The gamma size distribution typically used in RAMS (Flatau et al. 1989; Verlinde et al. 1990) reduces to

$$f_{\text{gam}}(D) = \frac{1}{D_{\text{mean}}} \exp\left(-\frac{D}{D_{\text{mean}}}\right) \tag{1}$$

for the Marshall–Palmer size distribution, where $f_{\text{gam}}(D)$ is the probability density function for the gamma distribution, and which represents the fraction of total hydrometeors of a given category per unit increment of diameter D, and D_{mean} is the mean diameter of the distribution. Multiplying the probability density function by the total number concentration (N_t) then gives the number density distribution $n(D)$:

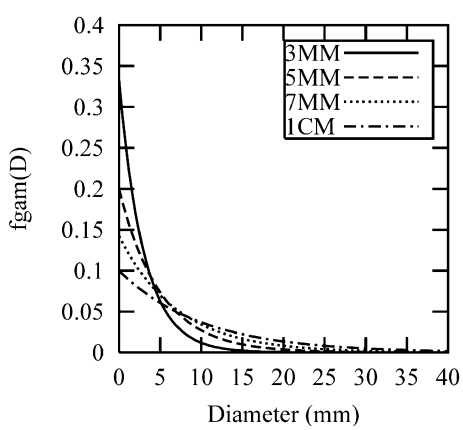

FIG. 2. The hail size distribution curves used for the 3MM (solid), 5MM (dash), 7MM (dot), and 1CM (dashed–dotted) sensitivity tests.

$$n(D) = N_t f_{\text{gam}}(D). \tag{2}$$

To determine the sensitivity of simulated supercell storm characteristics to changes in the mean hail diameter four simulations were conducted in which mean hail diameters of 3 mm, 5 mm, 7 mm, and 1 cm were used. The simulations were otherwise identical. These sensitivity tests will be referred to as the 3MM, 5MM, 7MM, and 1CM tests, respectively.

The impact of varying the mean hail diameter on the hail size distribution utilized in RAMS is shown in Fig. 2. Increasing the mean hail diameter from 3 mm to 1 cm results in the use of a hail size distribution in which the number concentration of smaller hailstones is reduced, and the number concentration of larger hailstones is increased. Assuming a fixed hail mixing ratio, the total number concentration is ~37 times greater in the 3MM case than in the 1CM case. Increasing the mean hail diameter also results in the mean terminal velocity for hail being approximately 1.8 times greater in the 1CM case, compared with that in the 3MM simulation. This will decrease the hail residence time at a specific model level in the larger-diameter cases and reduce the time for melting and evaporative processes to occur between the melting level and the ground.

Complete melting of a hailstone is predominantly mass dependent. However, the transfer of heat needed for melting is a surface process, and surface area therefore has an impact on melting rates. The mean surface-area-to-volume ratio is approximately 3.3 times greater in the 3MM case than in the 1CM case, assuming that the hailstone is spherical. The greater surface-area-to-volume ratios in the small hail cases imply that, for the same water content, the rate of hail melting and sub-

sequent evaporation of water off the hail surface will be greater in these cases.

Observations reported in the literature indicate that the intercept parameters for graupel and hail range from 10^3 to greater than 10^8 m^{-4}, with those for hail occurring toward the lower end of the range (Dennis et al. 1971; Federer and Waldvogel 1975; Knight et al. 1982) As the mean hail diameter is held fixed in each sensitivity test described here, the number concentration intercept parameter is diagnosed based on the prognosed mixing ratio. The diagnosed intercept parameters in the 3MM, 5MM, and 7MM cases range from 10^3 to 10^5 m^{-4}, respectively, which is in keeping with observations. The intercept parameter values diagnosed in the 1CM case are predominantly 10^2 m^{-4} in magnitude. While this falls just beyond the observed intercept parameters, none of the observations reported in the literature appear to be for supercell storms, which are frequently associated with large hail. It was therefore felt that using a mean hail diameter of 1CM was reasonable.

The changes in number concentrations, terminal fall speeds, and the surface-area-to-volume ratios caused by the progressive variations in the mean hail diameter will affect the rate of cooling within the storm and at the surface due to melting and evaporation. This in turn is expected to have a significant impact on the dynamic, thermodynamic, and precipitation characteristics of the developing simulated storms, and it is the range in these effects that we will now examine. It should be noted that on occasion, in the interests of brevity, only the 3MM and 1CM results will be compared as they represent the extremes of the hail diameter spectrum being tested here.

3. Mean hail diameter sensitivity tests

a. Storm development and movement

The storm tracks for the four mean hail diameter sensitivity tests are shown in Fig. 3. Storm splitting is evident by about 30 min in all simulations. After this time, differences in the development of both the right-moving (RM) and left-moving (LM) storms become apparent. In the 3MM, 5MM, and 7MM cases, the LM storm dissipates after about 45 min of simulation time. In the 1CM simulation, the LM storm exists for most of the simulation in spite of the clockwise curvature of the hodograph below 2 km (Klemp and Wilhelmson 1978b). Johnson et al. (1993) also noticed differences in the longevity of the LM storms in their ''ice'' versus ''no ice'' simulations—the LM was longer-lived in the ice simulation. The reasons for the longevity and development of the LM storm is the topic of a paper currently in preparation and will not be discussed here.

The RM storm is favored over the LM in all four sensitivity tests, which is in keeping with the low-level (below 2 km AGL) veering of the hodograph (Klemp and Wilhelmson 1978b). In the 3MM and 5MM simulations the RM updraft develops rapidly after storm splitting, reaching its maximum strength around 60 min. After this time, the RM in both cases begins to weaken as the low-level (below 2 km AGL) updraft undergoes an occlusion-like process. The updraft then redevelops. In the 7MM case, the RM starts to weaken after 90 min, while in the 1CM case, the RM updraft becomes strong and steady after about an hour, and shows relatively little change in width and strength throughout the rest of the simulation. Simply changing the mean hail diameter therefore has a significant effect on the strength, steadiness, and longevity of both the RM and LM storms.

b. Upper-level dynamic characteristics

Differences in the storm intensities between the four simulations may be seen by examining the maximum vertical velocity after approximately 40 min once the storms have reached a quasi-steady state (Fig. 4). The strongest updrafts range between 55 and 65 m s^{-1}. These magnitudes are similar to those simulated by Johnson et al. (1993) in their simulation of a supercell, and also compare favorably with those observed by Bluestein and Woodall (1990). Even though the updrafts in the 3MM and 5MM cases are the strongest of all four cases they soon collapse, while the more steady nature of the updrafts in the 7MM and 1CM cases is again obvious.

c. Low-level dynamic and thermodynamic characteristics

An important control on the strength of low-level downdrafts is the size and phase of the precipitation (e.g., Kamburova and Ludlam 1966; Betts and Silva Dias 1979; Srivastava 1987; Knupp 1988). Melting of the ice phase can contribute significantly to the cooling of the downdraft (Srivastava 1987; Knupp 1988). Knupp found that in convective High Plains storms melting can account for 10%–60% of the total cooling within certain downdrafts with evaporative cooling making up the difference, and that the melting contribution becomes greater when cloud bases are lower and the subcloud layer is moister, both of which inhibit evaporative cooling.

In the simulations presented here, the cloud bases (defined as the height above the surface where cloud water first exceeds 0.1 g kg^{-1}) are relatively low. They vary from approximately 1100 m AGL in the early stages of the 3MM, 5MM, and 7MM cases to approximately 1700 m AGL toward the end of the simulations, and from 1300 to 1700 m AGL in the 1CM simulation. The subcloud layer is moist, and the melting level occurs at ~4 km AGL. The more rapid melting rates and the smaller terminal fall velocities in the smaller hail cases generate stronger low-level (below 1 km AGL) downdrafts throughout most of the simulation than those in the large hail cases (Fig. 4), and result in less hail reach-

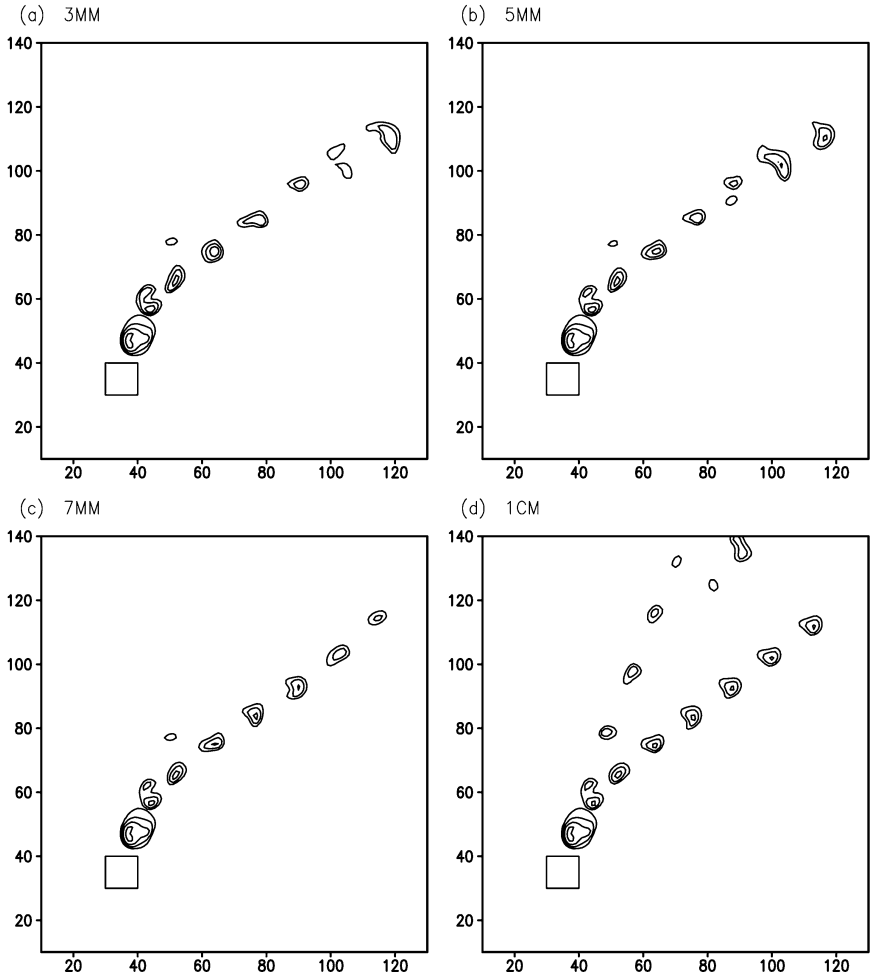

FIG. 3. Storm tracks of the (a) 3MM, (b) 5MM, (c) 7MM, and (d) 1CM simulations. The field shown is vertical velocity (contour interval is 10 m s^{-1}, starting at 10 m s^{-1}) at ~4800 m AGL. Storm positions are shown at 15-min intervals starting from the southwest grid corner. The axes are distance (km) from the southwest grid point for all figures unless otherwise indicated. The square box indicates the initial position and size of the warm bubble.

ing the surface (Fig. 5). Also, as the smaller hailstones melt more quickly they produce rain (through shedding or complete melting) more rapidly, and hence greater rates of evaporative cooling are achieved than in the larger hail runs. Varying the mean hail diameter from 3 mm to 1 cm, therefore, results in low-level downdrafts that are generally 20% stronger and 95% to 100% less hail at the surface.

The cold pool originates through the transport of cold air by the downdrafts to the surface, after which it is forced to diverge through continuity arguments. The strength of the cold pool increases as the mean hail diameter is decreased (Fig. 6). The 5MM and 7MM cases are not shown, but the trend is continuous between the 3MM and 1CM case. In the 3MM case, the strength of the cold pool decreases between 60 and 120 min following the collapse of the updrafts between 60 and 100 min (Fig. 4), the subsequent reduction in hail production between 70 and 110 min (Fig. 5), and the associated weakening in the downdrafts during the same time period (Fig. 4). In the 1CM case the relatively constant updraft, hail production and low-level downdrafts result in relatively constant cold pool temperatures between 60 and 120 min. The greatest cold pool potential temperature perturbations at 60 min differ by as much as 6 K between the 3MM and the 1CM cases, but are similar by 120 min. In the 1CM simulation the cold pool development associated with the LM may also be seen.

The depth of the cold pool (assuming that the top of the cold pool occurs at $\theta'/\theta_0 = 0$, where θ' is the perturbation potential temperature within the cold pool and θ_0 is the base-state potential temperature) also increases as the mean hail diameter is reduced due to the deeper (~3200 m AGL for the 3MM case, ~2500 m AGL for the 1CM case), colder, stronger low-level downdrafts in the smaller hail cases. In all four simulations, the cold pool is either close to or extends above the cloud base

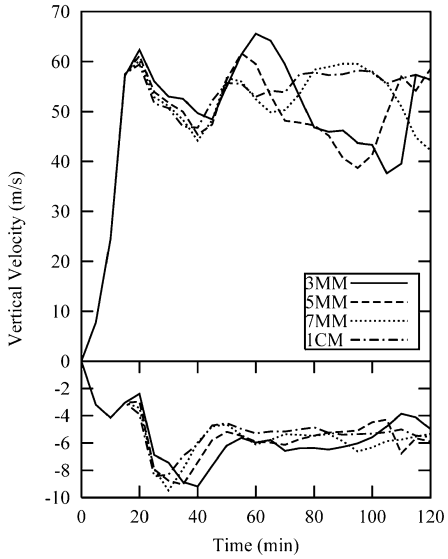

FIG. 4. Maximum updraft and downdraft strength (below 1 km AGL) for the RM storm as a function of time for the 3MM (solid), 5MM (dash), 7MM (dot), and 1CM (dashed–dotted) cases.

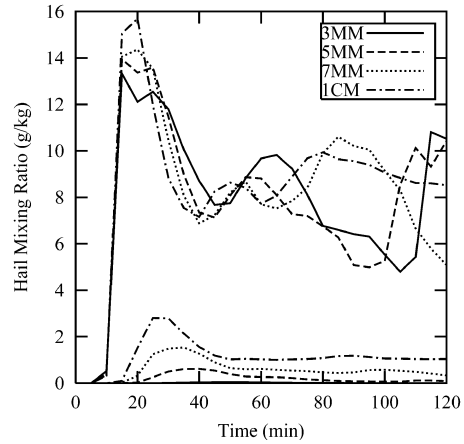

FIG. 5. Maximum hail mixing ratio (g kg^{-1}) throughout the domain (upper curves) and maximum hail mixing ratio at the surface (lower curves) for the 3MM (solid), 5MM (dash), 7MM (dot), and 1CM (dashed–dotted) cases.

highlighting the importance of melting in the development of the low-level downdrafts and associated cold pools, as evaporative processes are inhibited within the cloud itself. The deeper, more intense cold pools in the smaller hail cases propagate more rapidly than those in the larger hail cases (Fig. 6), which is in keeping with density current propagation theory (e.g., Rotunno et al. 1988). By 90 min, the faster outward-moving cold pool in the 3MM case covers ~7900 km^2, whereas the slower-propagating 1CM cold pool covers less than ~5000 km^2.

It was shown in the previous section that, while the updrafts in the large hail diameter cases increase slowly and steadily, those in the smaller hail cases achieve their maxima around 60 min, after which they rapidly collapse before redeveloping toward the end of the simulation (Fig. 7). This is caused by the differences in the depth and strength of the downdrafts and the associated convergence. In the small hail cases, the stronger downdrafts force the low-level gust front to surge eastward more rapidly than in the larger hail cases (Fig. 6). The rapid eastward movement of the gust front initially enhances convergence of the environmental air into the low levels (below 1 km AGL) of the storm between 50 and 60 min (Figs. 7a,c), thereby increasing the strength of the updraft during this time (Fig. 4). However, as the gust front continues to surge eastward between 60 and 70 min, it starts to outrun the updraft at midlevels (between 2 and 6 km AGL), and the low-level downdraft begins to wrap around the updraft in an occlusion-like process (Fig. 8a). As a result, convergence into the low-level updraft is reduced, while that along the gust front starts to increase (Fig. 7a). The reduced convergence and influx of warm, moist air into the low-level updraft cause the updraft to collapse (Fig. 4). In the larger hail cases, the gust front remains in close proximity to the updraft as a result of the weaker downdrafts and less intense cold pool (Fig. 8b). The downdraft does not occlude the updraft, and the convergence of warm, moist air in the lower regions of the updraft increases slowly (Figs. 7b,d). The steady increase of the updraft strengths in the larger hail cases between 50 and 80 min is therefore forced by a similar trend in the low-level convergence. Changing the mean hail diameter from 3 mm to 1 cm, therefore, significantly affects the strength of the low-level downdrafts and cold pool, the depth of the cold pool, the propagation speed of the gust front, and the low-level convergence in the region of the updraft.

d. Storm structure and precipitation characteristics

Horizontal cross sections through the midlevel (~5 km AGL) of the storm at its strongest stage reveal a single updraft structure in each case (Fig. 9). Each updraft is embedded within a mesocyclone, a characteristic typical of supercell storms (Doswell 1985). The mesocyclone strengths range from 0.015 s^{-1} for the 1CM case to 0.02 s^{-1} for the 3MM case, and the mesocyclone extends throughout most of the depth of the storm, both of which meet commonly accepted mesocyclone and supercell criteria (e.g., Brandes 1984; Johns and Doswell 1992; Doswell and Burgess 1993; Moller et al. 1994; Markowski and Straka 2000). A well-defined hook and a weak echo region (WER; bounded at higher levels) are evident in the horizontal cross section through the condensate field of the 3MM case (Fig. 10a). Such features are characteristic of supercell storms, although they do not always occur (Doswell and Burgess 1993). The bounded weak echo region (BWER) and overhang are apparent in the vertical cross section through the hail mixing ratio field (Fig. 10b). They are facilitated by the small hail size, which allows for more rapid vertical transport and easier movement around the

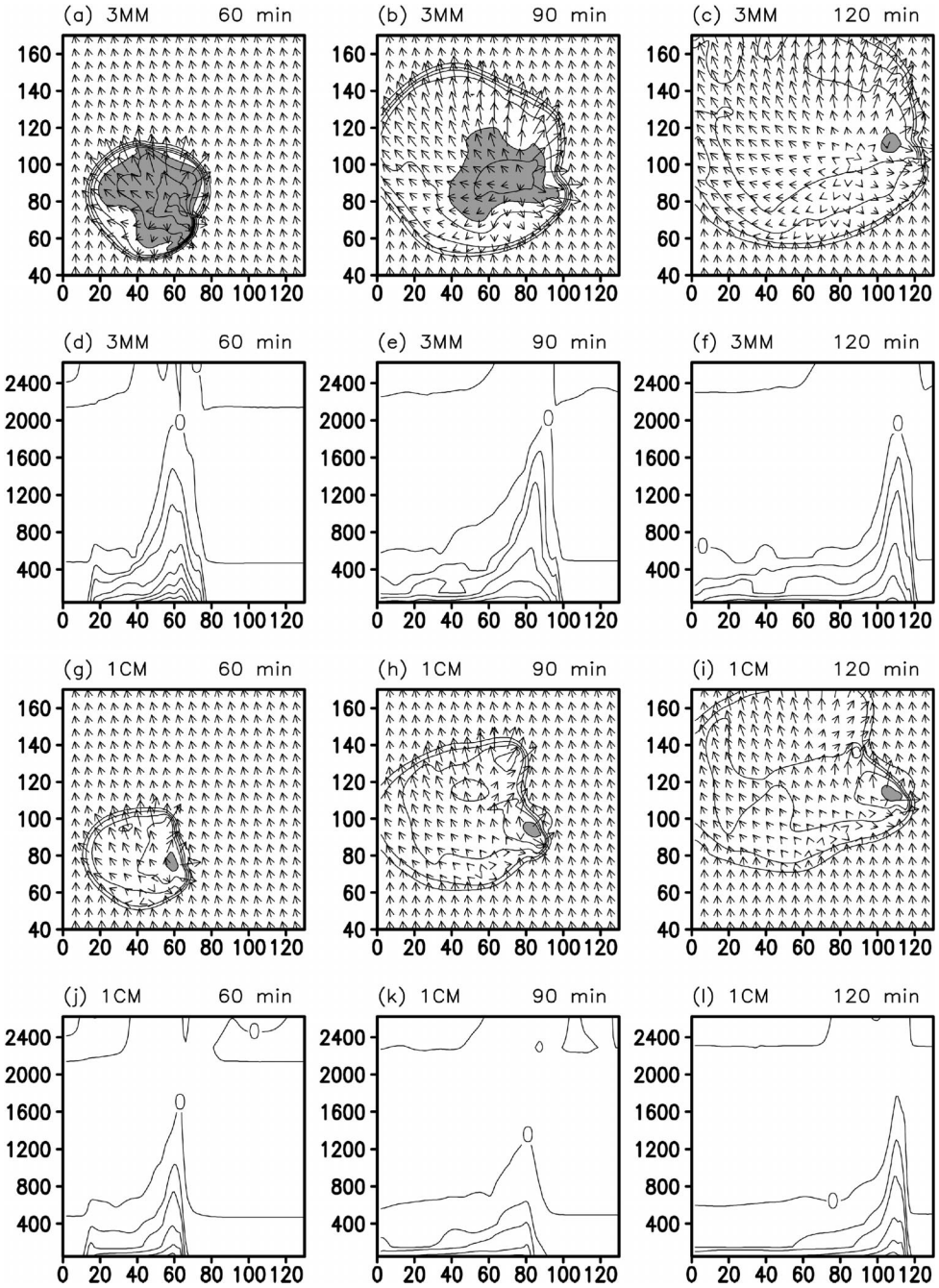

FIG. 6. Horizontal cross sections through the perturbation potential temperature (contour interval is 2 K starting at −2 K; −1-K isotherm also shown) and ground-relative wind vectors (plotted at every seventh grid point, 0.1 inch = 20 m s^{-1}) at 60, 90, and 120 min at 48 m AGL for the (a)–(c) 3MM and (g)–(i) 1CM cases. Vertical east–west cross sections through the perturbation potential temperature (contour interval is 2 K starting at 0 K; −1-K isotherm is also shown) are taken through the coldest region of the cold pool for the (d)–(f) 3MM and (j)–(l) 1CM cases. The vertical axis in (d)–(f) and (j)–(l) is height (m). Shading in (a)–(c) and (g)–(i) indicates regions in which the perturbation potential temperature is less than −8 K.

mesocyclone. The BWER is about 1500 m deep. Only a small indentation is visible in the 1CM horizontal condensate field (Fig. 10c), and a weak overhang is evident in the vertical cross section (Fig. 10d).

Cross sections through the 3MM and 1CM RM storms at their strongest stage also reveal numerous supercell characteristics (Fig. 11). An overshooting top is evident in both of the simulations, which results from the strong updraft-carrying air parcels above the equilibrium level. A large anvil extends both upshear and downshear of

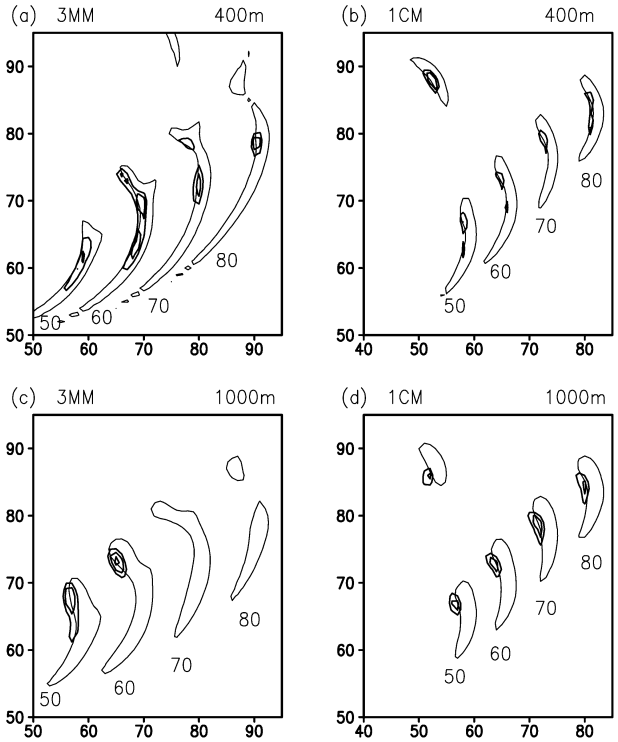

FIG. 7. Time progression of the convergence (thick lines; isolines are 0.007 and 0.008 s^{-1} for 400 m AGL; and 0.005, 0.006, and 0.007 s^{-1} for 1000 m AGL) and vertical velocity (thin lines; contour interval is 3 m s^{-1} for 400 m AGL, and 4 m s^{-1} for 1000 m AGL) at 400 m AGL for the (a) 3MM and (b) 1CM cases, and at 1000 m AGL for the (c) 3MM and (d) 1CM cases. The fields are shown at 50, 60, 70, and 80 min (left to right). Numbers on the plots indicate time in minutes.

the updraft in both cases, and a feature resembling a shelf cloud may be seen at the lower levels. Both simulations demonstrate the flow structure shown in Browning's (1964) supercell model. Low-level (<~2 km AGL) flow enters the storm from the south and east and rises in the updraft. Midlevel (~2 to ~10 km AGL) air enters the updraft from the south, and the updraft diverges at the tropopause level from where the majority

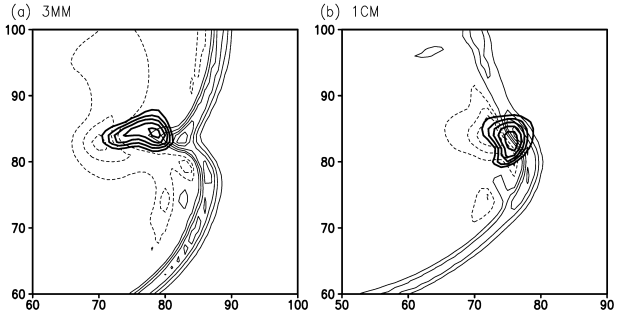

FIG. 8. Vertical velocity at ~48 m AGL (thin lines; contour interval is 0.3 m s^{-1}) and 4800 m AGL (thick lines; contour interval is 5 m s^{-1}, starting at 5 m s^{-1}) at 70 min for the (a) 3MM and (b) 1CM cases. Dashed lines indicate negative values; solid lines indicate positive values, and 0 isolines are excluded.

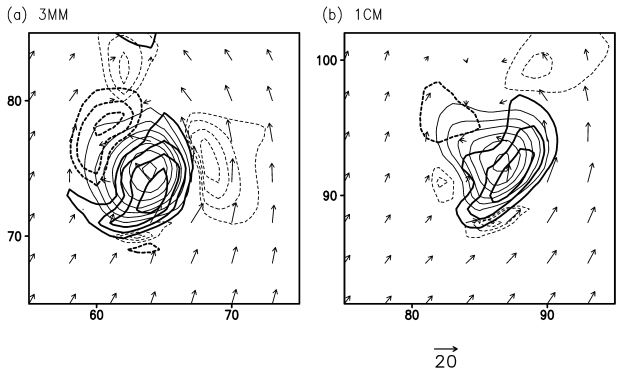

FIG. 9. Vertical velocity (thin lines; contour interval is 5 m s^{-1} for the updrafts, 1 m s^{-1} for the downdrafts), vertical vorticity (thick lines; contour interval is 0.005 s^{-1}), and storm-relative wind vectors at ~4800 m AGL at 60 min for the (a) 3MM case, and at 90 min for the (b) 1CM case. The wind vectors (m s^{-1}) are plotted at every third grid point and the vector scale is indicated at the bottom of the figure. Dashed lines indicate negative values, solid lines indicate positive values, and 0 isolines are excluded.

of the outflow moves eastward with the upper-level (>~10 km AGL) westerlies.

The storm heights are comparable between the two cases, but the 3MM storm is significantly wider than

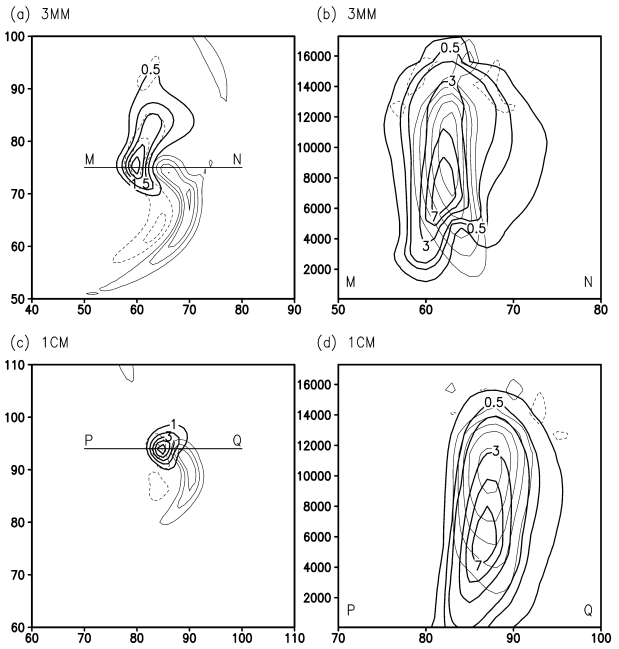

FIG. 10. Horizontal cross sections at ~1000 m AGL of the vertical velocity (thin lines; contour interval is 2 m s^{-1}) and condensate mixing ratio [thick lines; contour interval is 0.5 g kg^{-1} in (a) and 1 g kg^{-1} in (c)] for (a) 3MM case and (c) 1CM case. Vertical cross sections through the vertical velocity (thin lines; contour interval is 10 m s^{-1}) and hail mixing ratio (thick lines; contour interval is 2 g kg^{-1}, starting at 1 g kg^{-1}; the 0.1 and 0.5 g kg^{-1} isolines are also included) for the (b) 3MM case and (d) 1CM case. Dashed lines indicate negative values, solid lines indicate positive values, and 0 isolines are excluded. The lines MN in (a) and PQ in (c) indicate where the cross sections in (b) and (d) were taken, respectively.

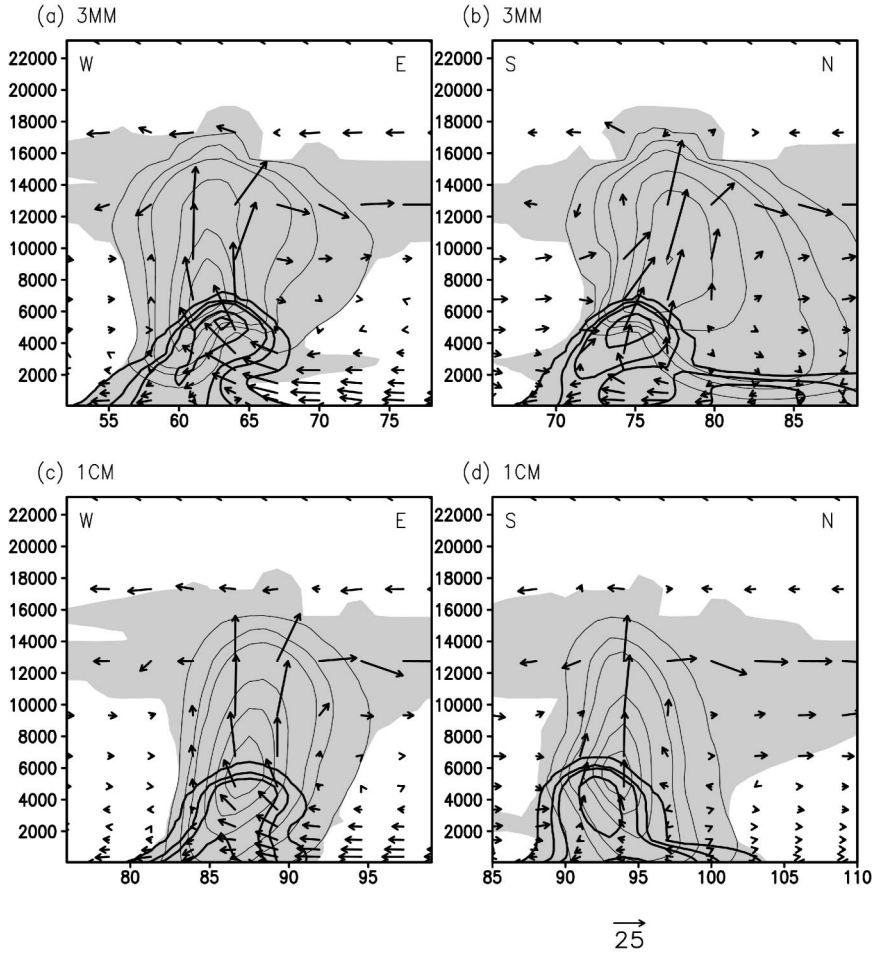

FIG. 11. (a), (c) East–west and (b), (d) north–south cross sections showing the precipitation characteristics of the RM storm for the 3MM case at 60 min and the 1CM case at 90 min, respectively. Shading indicates regions in which the condensate mixing ratios are greater than 0.1 g kg^{-1}. Hail mixing ratios are plotted using thin lines and rain mixing ratios using thick lines. The storm-relative winds vectors (m s^{-1}) are plotted at every third grid point, the magnitudes of which are indicated below the figure. The contour interval for all the mixing ratios is 2 g kg^{-1}, starting at 1 g kg^{-1}. The 0.1 and 0.5 g kg^{-1} mixing ratio isolines are also shown.

the 1CM storm. The small hail size in the 3MM case allows for it to be transported farther to the north and east of the core of the updraft than in the 1CM case. The vertical distribution of hail is also greater in the 3MM case. As a result of the greater transportability of small hail, the rainfall, which results primarily from melting and shedding, extends farther from the updraft core in the 3MM case than in the 1CM run where the rain, hail, and the updraft are closely collocated. The wider distribution of precipitation in the 3MM case generates a more expansive rear flank downdraft (RFD) and forward flank downdraft (FFD) than in the 1CM run (Fig. 8). Although the maximum accumulated rainfall is similar in all four cases, the accumulated rainfall at the surface extends over a greater area in the smaller hail cases (Fig. 12). The maximum accumulated hail is significantly greater in the larger hail cases (Fig. 12). Finally, the maximum accumulated precipitation (rain, snow, aggregates, graupel, and hail) increases as the mean hail diameter increases (not shown). Changes in the hail size distribution therefore have a significant effect on the amount and distribution of hail and rain, both vertically and horizontally, as well as on the storm structure.

e. Low-level vertical vorticity

As the mean hail diameter decreases, so the low-level vertical vorticity within the RM storm increases (Fig. 13). The maximum vertical vorticity in the 3MM case almost reaches 0.02 s^{-1} around 75 min and then decreases, whereas the maximum vertical vorticity in the 1CM is ~0.015 s^{-1} but remains steady. A detailed analysis of the factors affecting the low-level vertical and horizontal vorticity has been performed, the results of which have been included in a paper being prepared for

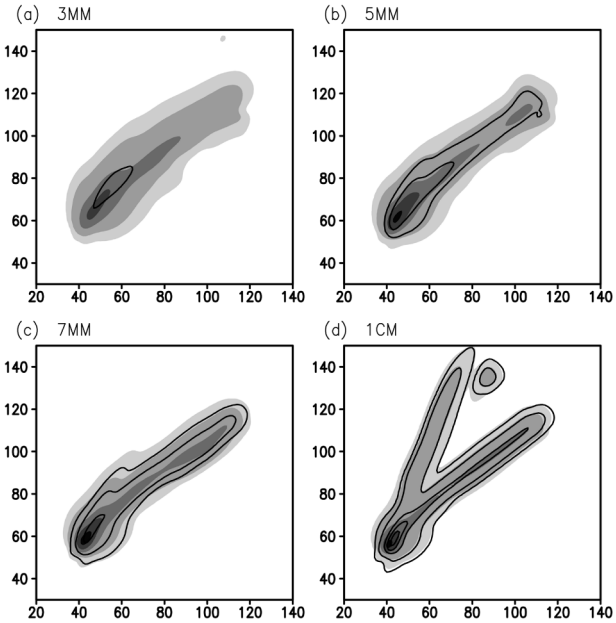

FIG. 12. Accumulated rainfall (mm, shading) and hail (mm, lines) at the surface over the 2-h simulation period for all four cases. Plotting intervals are 0.1, 1, 10, 20, 30, 40, and 50 mm for both rain and hail. Greater accumulations of rain are indicated by progressively darker shading.

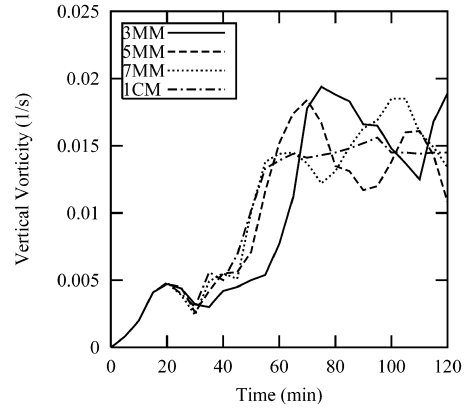

FIG. 13. Maximum vertical vorticity (s^{-1}) near the surface as a function of time for the 3MM (solid), 5MM (dash), 7MM (dot), and 1CM (dashed–dotted) simulations.

publication. However, some of the findings will be briefly summarized here.

Several factors appear to contribute to the differences in the low-level vertical vorticity between the 3MM and 1CM cases. The first factor is the difference in the propagation speeds of the gust front and cold pools (Figs. 14a,b). The stronger westerly to northwesterly flow behind the gust front in the 3MM case, compared with that in the 1CM case, results in greater horizontal wind shear and subsequently stronger vertical vorticity along the gust front, where this flow meets the southerly to southeasterly environmental air. The second factor affecting the low-level vertical vorticity differences are the stronger horizontal temperature gradients along the edge of the cold pool in the 3MM case compared with that in the 1CM case (Fig. 6, Figs. 14a,b). The stronger temperature gradients generate stronger horizontal vorticity through baroclinic forcing. Relatively strong horizontal vorticity is also generated along the eastern edge of the forward flank downdraft in the 3MM case due to baroclinic forcing, but is much weaker in the 1CM case (not shown).

Another factor affecting the low-level vertical vorticity involves the strength of the low-level (below 1 km AGL) downdraft. The mesohigh that forms in the 3MM simulation due to both the greater deceleration of the stronger, low-level downdrafts and the hydrostatic effect is stronger and covers a larger area than in the 1CM case (Figs. 14c,d). The greater divergence associated with the stronger mesohigh in the 3MM case results in faster flow away from the FFD toward the updraft and subsequent stronger convergence within the region of the updraft (Fig. 14c). This low-level convergence enhances the low-level vertical vorticity through stretching effects. The convergence within the region of the 1CM updraft is much weaker (Fig. 14d). The rapid outflow from the mesohigh in the 3MM case also enhances the horizontal streamwise vorticity in the inflow region to the north of the updraft through stretching effects. This is not obvious in the 1CM case (Figs. 14c,d). The tilting of horizontal vorticity by the updraft occurs in both cases. However, the enhanced horizontal vorticity in the 3MM case, as well as the greater stretching of the low-level vertical vorticity following the tilting in this case, lead to stronger low-level vertical vorticity compared with the 1CM case.

Should the relationship between hail size and vertical vorticity prove robust, it may explain why High Plains thunderstorms often produce large quantities of hail but are not frequent tornado producers. The relationship would also have implications for cloud seeding to suppress hail.

f. Storm type

Many of the features of the 3MM RM storm are characteristic of a typical classic (CL)-type supercell (Browning 1964; Lemon and Doswell 1979). These include moderate amounts of precipitation at the surface, little precipitation within the mesocyclone, a hook in the condensate field, and a BWER (Figs. 15a,c). As the mean hail diameter is increased so the storm features become more typical of an high-precipitation (HP)-type supercell (Doswell et al. 1990; Moller et al. 1994). These include heavy precipitation at the ground, substantial precipitation near and within the mesocyclone, and an almost indistinguishable hook and WER (Figs. 15b,d). Also, as the low-level vertical vorticity is strongest in the smaller hail cases, this lends support to the

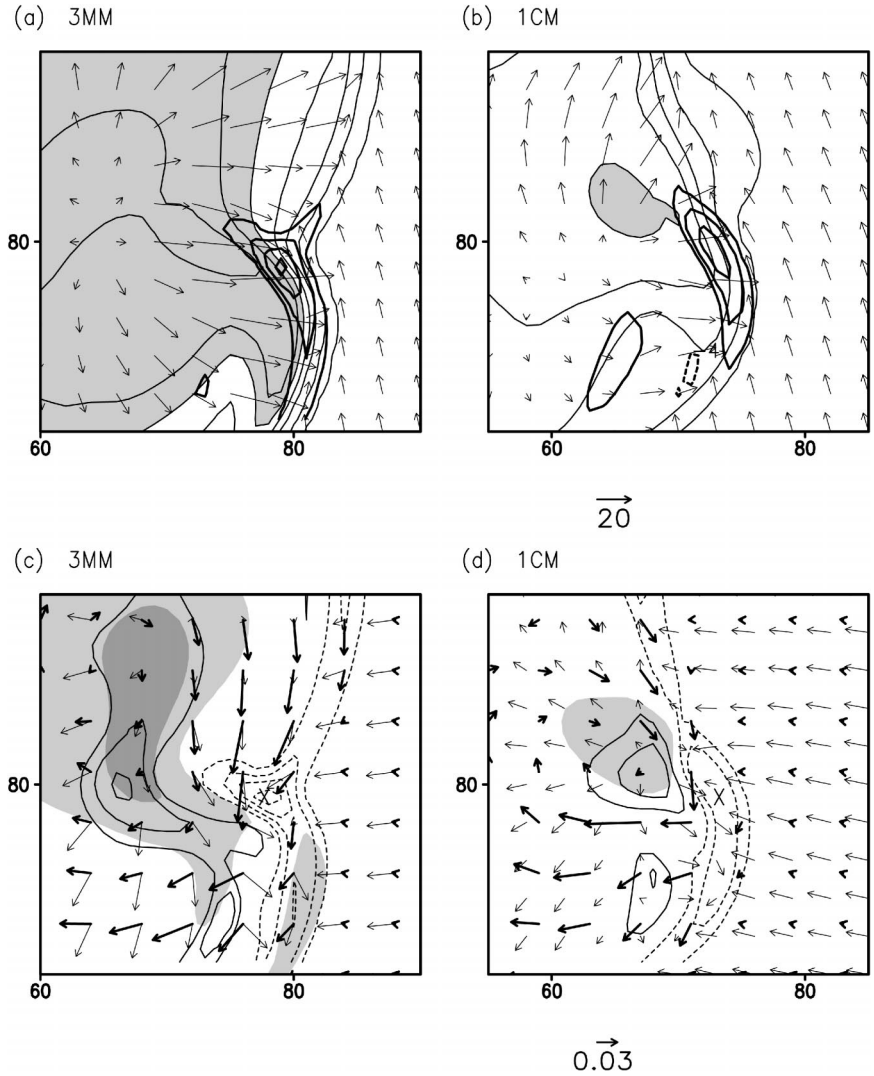

FIG. 14. Ground-relative wind vectors (plotted at every third grid point), perturbation potential temperature (thin lines, interval 2 K starting at −2 K; −1-K isotherm also shown) and vertical vorticity (thick lines, interval 0.005 s^{-1}) at ~48 m AGL for (a) 3MM and (b) 1CM cases at 70 min. Regions in which the perturbation potential temperature is less than −8 K are shaded. The magnitude of the wind vectors (m s^{-1}) is indicated below (b). Storm-relative wind vectors (thin, plotted at every fourth grid point), horizontal vorticity vectors (thick, plotted at every fourth grid point), perturbation Exner function (shaded; light shading > 0.4, dark shading > 0.8), and the divergence (thin lines, interval 0.003 s^{-1}) for the (c) 3MM and (d) 1CM cases at ~150 m AGL at 70 min; "×" on (c) and (d) indicates the center of the updraft. The magnitude of the horizontal vorticity vectors (s^{-1}) is indicated below (d). Dashed lines indicate negative values, solid lines indicate positive values, and 0 isolines are excluded.

observational evidence that CL supercells are probably responsible for the majority of violent (F4–F5) tornadoes (Doswell and Burgess 1993). The results of these simulations suggest that the type of supercell that develops is influenced by the precipitation characteristics of the storm. This builds on several previous studies that have stressed the importance of the relationship between precipitation physics, storm dynamics, and storm type (e.g., Johnson et al. 1993; Brooks et al. 1994; Rasmussen and Straka 1998).

4. Discussion and conclusions

The purpose of the research presented in this paper was to investigate the sensitivity of simulated supercells to variations in the size spectrum of hailstones. Four sensitivity tests were conducted in which the hail size distribution was altered by progressively increasing the mean hail diameter from 3 mm to 1 cm. Increasing the mean hail diameter will increase the mean terminal fall speed and reduce the surface-area-to-volume ratios of

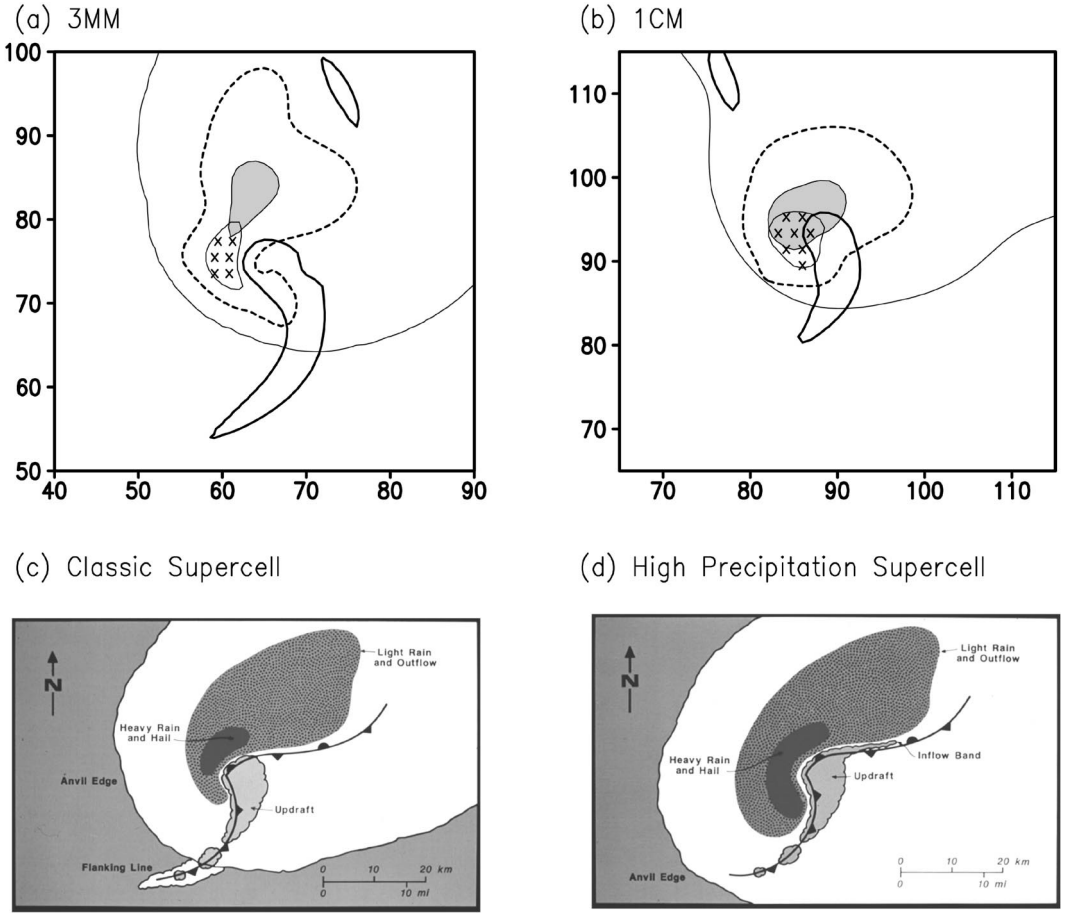

FIG. 15. Simulated storm characteristics from the (a) 3MM and (b) 1CM cases, showing the updraft (thick solid lines), heavy hail (shaded region), heavy rain ("×" regions), area of light rain (within the thick-dashed line), and the anvil (within the thin line); observed (c) CL and (d) HP supercell characteristics shown by a plan view of the precipitation (stippling), surface outflow boundaries (frontal symbols), updraft maxima (scalloped line), and cloud boundaries (also scalloped; after Doswell and Burgess 1993).

hail, both of which will reduce the rate of cooling due to hail melting and the subsequent evaporation of water off the hail surface. The results of the sensitivity tests demonstrate that numerous characteristics of the supercell storms that develop are sensitive to the size of the mean hail diameter. For smaller hailstone sizes, the low-level downdrafts are stronger; the cold pools are deeper, more intense, and faster moving, the LM is shorter lived; and the RM updrafts and low-level vertical vorticity achieve greater maxima but are not as steady as those in the larger hail runs. Also, in the smaller hail simulations, hail and rain are located at higher levels in the storm and farther away from the core of the updraft, and the total rainfall and hail at the surface occur over greater areas. In general, the maximum accumulated hail at the surface increases with increasing hail size. Finally, the hail size appears to influence the type of supercell that develops, with CL-type features being more typical when the mean hail diameter is small, and HP-type characteristics more prevalent in the larger hail cases.

The results of the mean hail diameter sensitivity tests suggest that a balance is needed between the precipitation characteristics of a storm and the low-level environmental inflow air if a long-lived, steady supercell storm is to develop. In the smaller hail cases, the low-level vertical vorticity is stronger. However, the greater rates of melting and evaporation result in stronger downdrafts, which force the gust front to outrun the updraft, thereby depriving the updraft of the influx of warm environmental air and weakening the storm. In the larger hail cases, while the gust front does not outrun the updraft as the downdrafts are weaker, the low-level vertical vorticity is not as strong. Strengthening the environmental inflow air in the smaller hail cases would prevent the gust front from outrunning the storm thereby enhancing its lifetime, while weakening the inflow in the larger hail cases would allow the gust front to propagate away from the updraft thereby reducing the storm longevity.

Finally, the demonstrated sensitivity of simulated supercell storms to the hail size distribution characteristics highlights two important aspects that need to be con-

sidered. First, when simulating deep convective storms, the parameters determining the hail size distribution need to be accurately specified or predicted. Small inaccuracies in the initial parameter settings could significantly change the dynamic, thermodynamic, or precipitation characteristics of the resultant storm. A control simulation was performed in which hail was excluded as a species (not shown). The differences in storm dynamics and behavior that occur as a result of variations in the mean hail diameter are equal in magnitude to those that occur as a result of excluding hail completely. Other hail and ice parameters may have similar effects, and this requires further investigation. The second consideration is that we need to gain a better understanding of the factors that influence the hail size distribution of observed storms. Such factors may include concentrations of CCN, GCCN, and IFN, the presence of dry layers, wind shear, and variations in the vertical velocity field.

Acknowledgments. The comments of the anonymous reviewers are appreciated. This work was funded by the National Science Foundation under Contract ATM-9900929.

REFERENCES

Betts, A. K., and M. F. Silva Dias, 1979: Unsaturated downdraft thermodynamics in cumulonimbus. *J. Atmos. Sci.,* **36,** 1061–1071.

Bluestein, H. B., and G. R. Woodall, 1990: Doppler-radar analysis of a low-precipitation severe storm. *Mon. Wea. Rev.,* **118,** 1640–1664.

Brandes, E. A., 1984: Vertical vorticity generation and mesocyclone sustenance in tornadic thunderstorms: The observational evidence. *Mon. Wea. Rev.,* **112,** 2253–2269.

Brooks, H. E., C. A. Doswell III, and R. B. Wilhelmson, 1994: The role of midtropospheric winds in the evolution and maintenance of low-level mesocyclones. *Mon. Wea. Rev.,* **122,** 126–136.

Browning, K. A., 1964: Airflow and precipitation trajectories within severe local storms which travel to the right of the winds. *J. Atmos. Sci.,* **21,** 634–639.

Chen, S., and W. R. Cotton, 1988: The sensitivity of a simulated extratropical mesoscale convective system to longwave radiation and ice-phase microphysics. *J. Atmos. Sci.,* **45,** 3897–3910.

Cotton, W. R., and Coauthors, 2003: RAMS 2001: Current status and future directions. *Meteor. Atmos. Phys.,* **82,** 5–29.

Dennis, A. S., P. L. Smith Jr., G. A. P. Peterson, and R. D. McNeil, 1971: Hailstone size distributions and equivalent radar reflectivity factors computed from hailstone momentum records. *J. Appl. Meteor.,* **10,** 79–85.

Doswell, C. A., III, 1985: The operational meteorology of convective weather. Vol. II, Storm scale analysis. NOAA Tech. Memo. ERL ESG-15, 240 pp.

——, and D. W. Burgess, 1993: Tornadoes and tornadic storms: A review of conceptual models. *The Tornado: Its Structure, Dynamics, Prediction, and Hazards, Geophys. Monogr.,* No. 79, Amer. Geophys. Union, 161–172.

——, A. R. Moller, and R. Przybylinski, 1990: A unified set of conceptual models for variations on the supercell there. Preprints, *16th Conf. on Severe Local Storms,* Kananaskis Park, AB, Canada, Amer. Meteor. Soc., 40–45.

Federer, B., and A. Walkvogel, 1975: Hail and raindrop size distributions from a Swiss multicell storm. *J. Appl. Meteor.,* **14,** 91–97.

Flatau, P. J., G. J. Tripoli, J. Verlinde, and W. R. Cotton, 1989: The CSU–RAMS Cloud Microphysical Module: General Theory and Code Documentation. Colorado State University Atmospheric Science Paper 451, 88 pp.

Gilmore, M. S., J. M. Straka, and E. N. Rasmussen, 2004: Precipitation uncertainty due to variations in precipitation particle parameters within a simple microphysics scheme. *Mon. Wea. Rev.,* in press.

——, ——, and ——, 2004: Precipitation and evolution sensitivity in simulated deep convective storms: Comparisons between liquid-only and simple ice and liquid phase microphysics. *Mon. Wea. Rev.,* in press.

Grasso, L. D., 2000: The dissipation of a left-moving cell in a severe storm environment. *Mon. Wea. Rev.,* **128,** 2797–2815.

Jewett, B. F., R. B. Wilhelmson, J. M. Straka, and L. J. Wicker, 1990: Impact of ice parameterization on the low-level structure of modeled supercell thunderstorms. Preprints, *16th Conf. on Severe Local Storms,* Kananaskis Park, AB, Canada, Amer. Meteor. Soc., 275–280.

Johns, R. H., and C. A. Doswell, 1992: Severe local storms forecasting. *Wea. Forecasting,* **7,** 588–612.

Johnson, D. E., P. K. Wang, and J. M. Straka, 1993: Numerical simulations of the 2 August 1981 CCOPE supercell storm with and without ice microphysics. *J. Appl. Meteor.,* **32,** 745–759.

Kamburova, P. L., and F. H. Ludlam, 1966: Rainfall evaporation in thunderstorm downdrafts. *Quart. J. Roy. Meteor. Soc.,* **92,** 510–518.

Klemp, J. B., and R. B. Wilhelmson, 1978a: The simulation of three-dimensional convective storm dynamics. *J. Atmos. Sci.,* **35,** 1070–1096.

——, and ——, 1978b: Simulations of right- and left-moving storms produced through storm splitting. *J. Atmos. Sci.,* **35,** 1097–1110.

Knight, C. A., W. A. Cooper, D. W. Breed, I. R. Paluch, P. L. Smith, and G. Vali, 1982: Microphysics. *Hailstorms of the Central High Plains,* C. A. Knight and P. Squires, Eds., Colorado Associated University Press, 151–193.

Knupp, K. R., 1988: Downdrafts within High Plains cumulonimbi. Part II: Dynamics and thermodynamics. *J. Atmos. Sci.,* **45,** 3965–3982.

Lemon, L. R., and C. A. Doswell III, 1979: Severe thunderstorm evolution and mesocyclone structure as related to tornadogenesis. *Mon. Wea. Rev.,* **107,** 1184–1197.

Markowski, P. M., and J. M. Straka, 2000: Some observations of rotating updrafts in a low-buoyancy, highly sheared environment. *Mon. Wea. Rev.,* **128,** 449–461.

Marshall, J. S., and W. M. Palmer, 1948: The distribution of raindrops with size. *J. Meteor.,* **5,** 165–166.

Meyers, M. P., R. L. Walko, J. Y. Harrington, and W. R. Cotton, 1997: New RAMS cloud microphysics parameterization. Part II: The two-moment scheme. *Atmos. Res.,* **45,** 3–39.

Moller, A. R., C. A. Doswell III, M. P. Foster, and G. R. Woodall, 1994: The operational recognition of supercell thunderstorm environments and storm structures. *Wea. Forecasting,* **9,** 327–347.

Pielke, R. A., and Coauthors, 1992: A comprehensive meteorological modeling system—RAMS. *Meteor. Atmos. Phys.,* **49,** 69–91.

Rasmussen, E. N., and J. M. Straka, 1998: Variations in supercell morphology. Part I: Observations of the role of upper-level storm-relative flow. *Mon. Wea. Rev.,* **126,** 2406–2421.

Rotunno, R., J. B. Klemp, and M. L. Weisman, 1988: A theory for strong, long-lived squall lines. *J. Atmos. Sci.,* **45,** 463–485.

Schlesinger, R. E., 1999: Heat, moisture, and momentum budgets of isolated deep midlatitude and tropical convective clouds as diagnosed from three-dimensional model output. Part II: Sensitivity to ice phase and small change in ambient shear strength and low-level moisture supply. *J. Atmos. Sci.,* **56,** 3520–3543.

Smagorinsky, J., 1963: General circulation experiments with the primitive equations I. The basic experiment. *Mon. Wea. Rev.,* **91,** 99–164.

Srivastava, R. C., 1987: A model of intense downdrafts driven by

the melting and evaporation of precipitation. *J. Atmos. Sci.,* **44,** 1752–1773.

Tartaglione, N., A. Buzzi, and M. Fantini, 1996: Supercell simulations with simple ice parameterization. *Meteor. Atmos. Phys.,* **58,** 139–149.

Verlinde, J., P. J. Flatau, and W. R. Cotton, 1990: Analytical solutions to the collection growth equation. Comparison with approximate methods and application to cloud microphysics parameterization schemes. *J. Atmos. Sci.,* **47,** 2871–2880.

Walko, R. L., W. R. Cotton, M. P. Meyers, and J. Y. Harrington, 1995: New RAMS cloud microphysics parameterization. Part I: The single-moment scheme. *Atmos. Res.,* **38,** 29–62.